Supplement of

First field deployment of VIA-NO_3-CIMS for molecular characterization and source apportionment of particle-phase oxygenated organic molecules in eastern China

Maoyu Cao et al.

Correspondence to: Yan Chao (chaoyan@nju.edu.cn)

Table of Content

S1 Characterization of the VIA-NO_3-CIMS System

The main components of the VIA-NO_3-CIMS system and the sampling configuration used in this study are illustrated in Fig. 1. A detailed evaluation of the system performance is presented in the following sections.

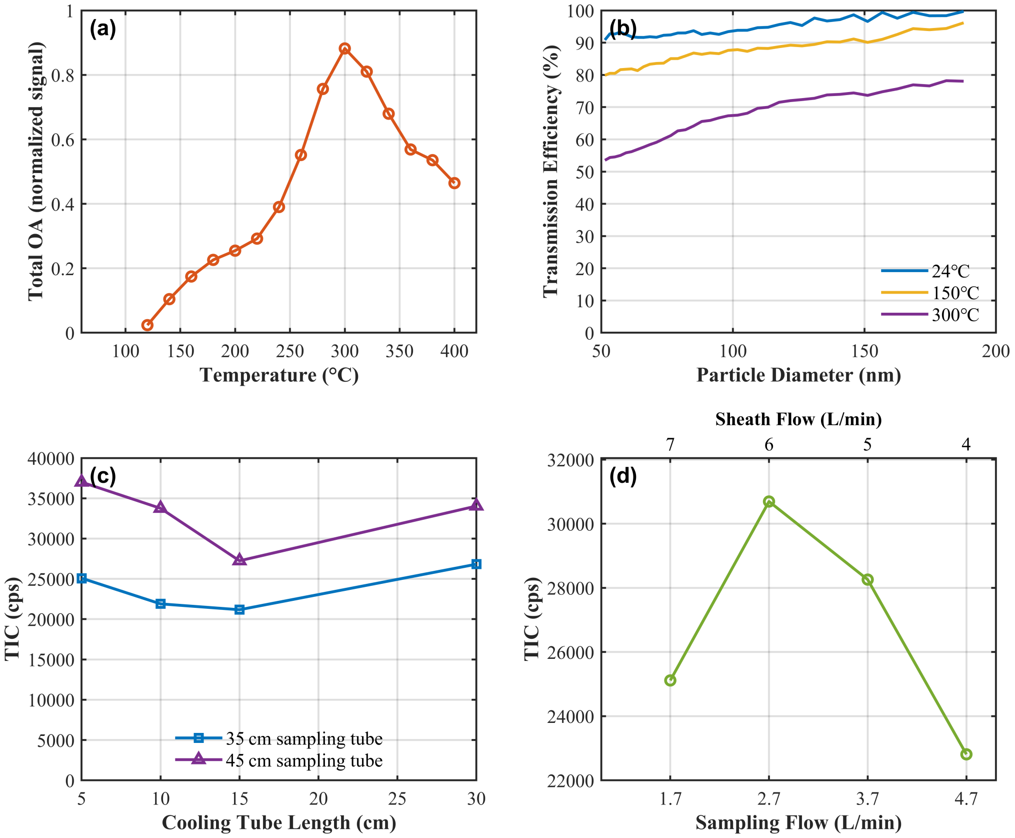

Figure S1. Optimization of operating parameters for the VIA-NO_3-CIMS system. (a) Response of the total OA signal as a function of evaporation temperature. (b) Particle transmission efficiency as a function of particle diameter measured at three evaporation temperatures (24, 150, and 300 °C). (c) Total ion current (TIC) obtained using different cooling tube lengths (5–15 cm) for two sampling tube configurations (35 and 45 cm). (d) TIC as a function of sampling flow rate.

S1.1 Determination of sampling temperature

In the VIA-NO_3-CIMS system, the temperature of the evaporation tube governs both the volatilization efficiency of particle-phase organics and their subsequent detection sensitivity via nitrate-ion chemical ionization. To assess this dependence, a linear temperature ramp from 120 to 400 °C was applied over a 30 min period, during which the OA in the ambient environment was continuously monitored. As shown in Fig. S1a, the OA signal increased steadily with temperature and reached a maximum at approximately 300 °C. This temperature was therefore identified as the optimum operating point and was subsequently adopted as the standard condition for all measurements, as it provided the highest overall OA signal under the experimental conditions. Nevertheless, it should be noted that different compounds exhibit distinct volatilization behaviors and may experience varying degrees of thermal decomposition and transmission losses during heating. Consequently, some losses are still expected at this temperature, particularly for more volatile compounds, and the measured molecular composition may be biased toward lower-volatility species.

S1.2 The transmission efficiency of particulate matter

To enhance the quantitative accuracy of organic aerosol measurements, particle transmission losses within the sampling line were first evaluated. NaCl particles were generated using an aerosol generator and sequentially introduced through the evaporation tube at temperatures ranging from ambient to 300 °C. Upstream and downstream particle size distributions and number concentrations were measured with a scanning mobility particle sizer (SMPS). As shown in Fig. S1b, the transmission efficiency exceeded 90% at room temperature but decreased substantially with increasing temperature. This decline is attributed to enhanced turbulence and stronger thermal gradients at elevated temperatures: turbulence-induced diffusion and Brownian motion drive smaller, low-inertia particles toward the tube wall, where thermophoresis and molecular diffusion promote their deposition. Consequently, transmission losses are most pronounced for the smallest particle diameters. It should be noted, however, that although higher temperatures enhance deposition, these losses are not expected to introduce a significant bias for volatile organic particles. Material deposited on the wall is likely to re-evaporate under sustained heating and subsequently undergo ionization and detection.

S1.3 cooling tube : sampling tube

Following thermal desorption at 300 °C, the resulting vapor was transported to the NO_3^- ionization region through a transfer line consisting of a cooling tube and a sample tube.

The dimensions of this transfer line can influence vapor transport and instrument sensitivity. Therefore, combinations of cooling-tube length (5–15 cm) and sample-tube length (35 and 45 cm) were systematically evaluated using the total ion current (TIC) as the performance metric (Fig. S1c).

As shown in Fig. S1c, the 45 cm sample tube consistently produced higher TIC values than the 35 cm configuration across all tested conditions. For the cooling tube, the 5 cm length yielded the highest overall TIC signal when combined with the 45 cm sample tube. This configuration (5 cm cooling tube + 45 cm sample tube) therefore provided the maximum signal intensity and was selected as the optimal transfer line setup for subsequent measurements.

S1.4 sampling flow : sheath flow

As shown in Fig. S1, an integrated sheath-flow module was installed downstream of the evaporation tube. A controlled stream of particle-free carrier gas was introduced around the sample flow to supplement the total inlet flow required by the NO_3^- ion source while establishing a stable laminar core within the transfer line. This configuration minimizes contact between the sample vapor and the tube wall and helps maintain stable flow conditions at the ion-source entrance. To optimize the balance between sample and sheath flows, we systematically varied their volumetric rates at an evaporation temperature of 300 °C and monitored the resulting TIC (Fig. S1d). Increasing the sample flow from 1.7 to 2.7 L min^{-1} enhanced the TIC, which reached a maximum at 2.7 L min^{-1}, corresponding to a sheath-flow rate of 6 L min^{-1}. Further increasing the sample flow to 3.7 L min^{-1} led to a decline in TIC, likely due to the reduced sheath flow weakening the laminar sheath and promoting vapor re-condensation and wall losses.

By jointly optimizing the evaporation temperature, the cooling-to-sample-line length ratio, and the sample-to-sheath-flow ratio, the following operating conditions were identified as optimal for the VIA-NO_3-CIMS system: an evaporation temperature of 300 °C, a 5 cm cooling tube, a 45 cm sample line, a sample flow of 2.7 L min^{-1}, and a sheath flow of 6 L min^{-1}. This configuration promotes efficient thermal desorption of particle-phase organics while introducing a sheath flow of nitrogen that rapidly dilutes the evaporated vapors and establishes a stable laminar flow field, thereby reducing vapor-wall interactions and transmission losses.

S1.5 Determination of particle evaporation efficiency

To quantify the evaporation efficiency of particle-phase organics in the VIA–NO_3–CIMS system under the optimized operating conditions, ambient aerosol particles were size-selected using an aerodynamic aerosol classifier (AAC) and introduced into the VIA inlet. Particle diameters of 50, 100, 200, 300, and 470 nm were sequentially selected to evaluate potential size-dependent effects. The number size distributions upstream and downstream of the evaporation tube were measured using a scanning mobility particle sizer (SMPS). For each selected size, measurements were conducted under two conditions: (i) with the evaporation tube unheated, serving as a reference, and (ii) with the evaporation tube operated at 300 °C, corresponding to the standard operating temperature used throughout this study. The evaporation efficiency was defined as the fractional reduction in particle volume upon heating, calculated as

$$\text{Evaporation efficiency} = 1 - V_{heated}/V_{bypass}$$

where V_{heated} and V_{bypass} denote the integrated particle volume measured by the SMPS with and without heating, respectively.

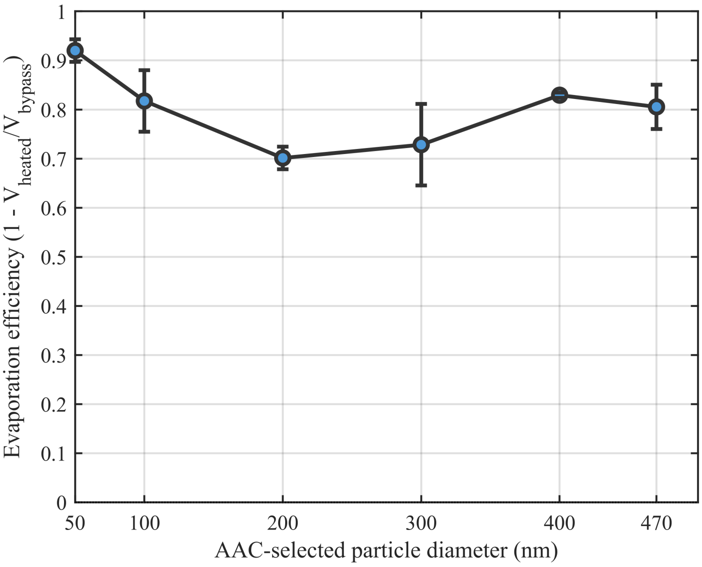

Figure S2. Size-dependent evaporation efficiency of the VIA-NO_3-CIMS system at 300 °C.

The resulting size-dependent evaporation efficiencies at 300 °C are summarized in Fig.

S2. Evaporation efficiencies ranged from approximately 70% to 92% across the investigated particle size range, with slightly lower values observed for intermediate particle diameters (~200 nm). The slightly lower evaporation efficiencies observed around 200 nm may reflect differences in particle composition and mass loading across particle sizes, as well as kinetic limitations associated with heat and mass transfer during thermal desorption. Overall, these results demonstrate that operation at 300 °C enables substantial volatilization of particle-phase organic material, while a residual non-volatile fraction remains.

S2 Availability analysis of trace gases in this study

During the observation period, trace-gas measurements were not available at the SORPES site (32°07′14″ N, 118°57′10″ E). Therefore, data from the Nanjing Xianlin University Town site (32°06′41″ N, 118°54′48″ E), located approximately 4 km away, were used as a substitute. Paired comparisons for the period 1 November–31 December 2024 show strong consistency between the two sites (Fig. S3): NO_2 (r = 0.81), O_3 (r = 0.91), and $PM_{2.5}$ (r = 0.91). Accordingly, the Xianlin dataset can be regarded as a representative and reliable substitute for the missing trace-gas record at SORPES, with minimal potential for systematic bias.

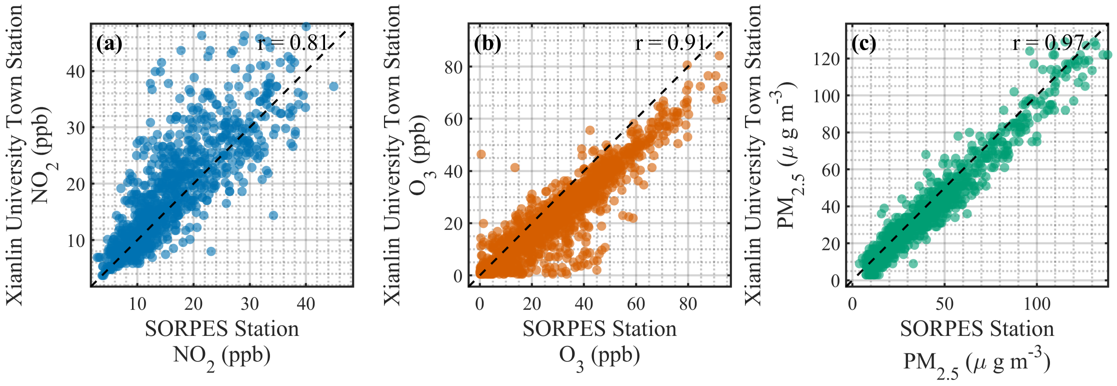

Figure S3: Paired scatterplots of NO_2, O_3, and $PM_{2.5}$ between the SORPES and Xianlin sites (in this study) for 1 November–31 December 2024.

S3 Qualitative analysis of oxygen-containing organic molecules

S3.1 binPMF inputs

In binPMF, as described in (Zhang et al., 2019), each high-resolution mass spectrum was first linearly interpolated onto a uniform 0.001 Th grid. For each nominal mass, data within −0.25 to +0.45 Th were re-binned at 0.004 Th intervals; only bins with signals above the noise threshold were retained, yielding approximately 175 bins per unit mass and substantially reducing the dimensionality. Bins corresponding to nominal masses outside the 200–400 Th range were subsequently excluded from the PMF input matrix. At each time step, the intensities of the retained bins (ions s^{-1}) were concatenated in ascending-mass order to form a column vector, and stacking these vectors sequentially over time generated a k × n bin-by-time data matrix.

The error matrix was calculated based on Eq. (1) (Polissar et al., 1998)

$$S_{ij} = \sigma_{ij} + \sigma_{noise}$$

where S_{ij} represents the uncertainty of m/z j at time i and σ_{ij} stands for counting-statistics uncertainty and is estimated as follows:

$$\sigma_{ij} = a \times \frac{\sqrt{I_{ij}}}{\sqrt{t}}$$

where I is the signal intensity term, in unit of ions/s, t is the averaging time in seconds, and a is an empirical coefficient that compensates for unaccounted uncertainties and equals 1.28 in this study, as previously determined from laboratory experiments (Allan et al., 2003; Yan et al., 2016). The σ_{noise} term was estimated as the median of the standard deviations of signals in bins located between nominal masses, where no physically meaningful signals are expected.

S3.2 Diagnostics for factor number determination

In this study, factor solutions ranging from 1 to 20 were explored using bin-PMF. The optimal number of factors was determined based on statistical diagnostics, including the ratio of Q to Qexp, the distribution of scaled residuals, and the overall reconstruction of mass spectral peaks. Rather than strictly emphasizing the physical interpretability of each factor, we allowed a relatively larger number of factors to ensure adequate fitting of the observed peaks. Accordingly, the resolved factors should be regarded primarily as mathematical constructs that enhance model performance, rather than as direct representations of distinct physical sources or processes. Ultimately, a 13-factor solution was selected as optimal. Fig. S4 shows the variation of Q/Qexp with the number of factors, the comparison between measured and reconstructed total spectral signals, and the factor–factor correlations (G-space plot). Fig. S5 presents the residual distributions for the 13-factor solution, further supporting the robustness of this choice. Fig. S6 displays the mass spectra, time series, and diurnal variations of the 13 resolved factors.

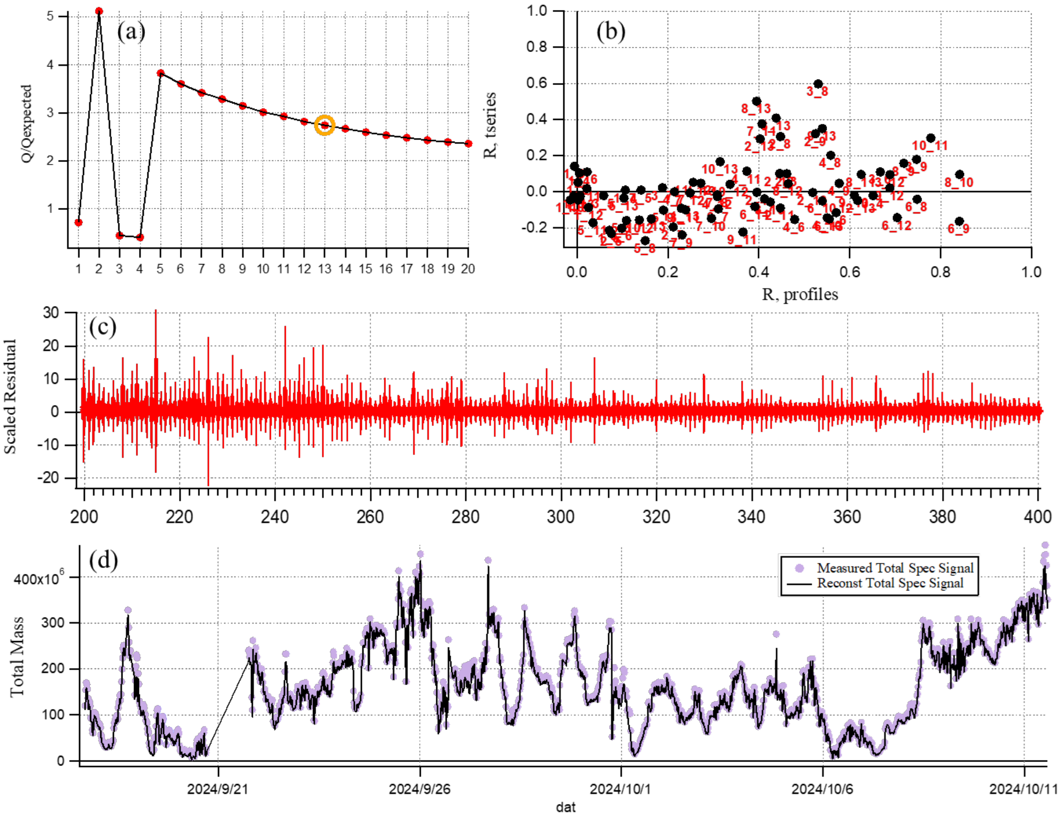

Figure S4. (a) Q/Qexp as a function of number of factors. (b) cross-correlation coefficients (R) of the time series and spectral profiles among the PMF factors. (c) the box and whiskers plot showing the distributions of scaled residuals for each m/z. (d) time series of the measured OA mass and the reconstructed OA mass

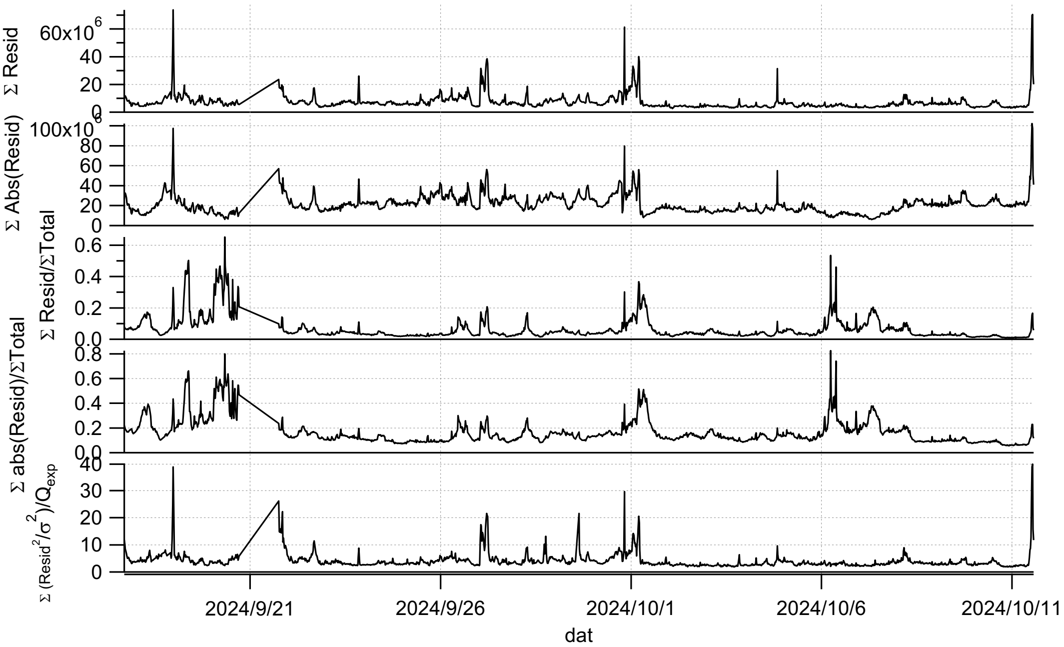

Figure S5. Distribution of scaled residuals for the 13-factor BinPMF solution.

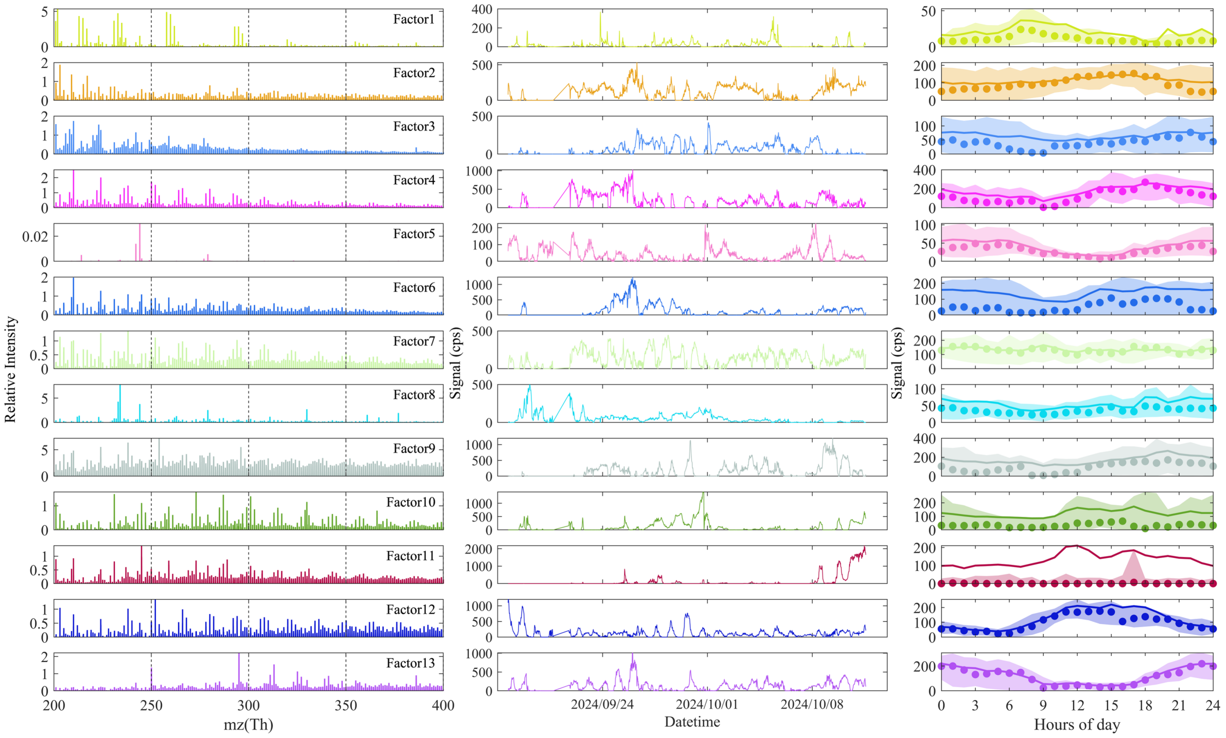

Figure S6. Solution with 13 factors from the binPMF analysis. For each factor (rows F1–F13), the left panel shows the factor profile (mass spectrum), the middle panel presents the corresponding time series, and the right panel illustrates the diurnal variation.

S4 Quantification of oxygen-containing organic molecules

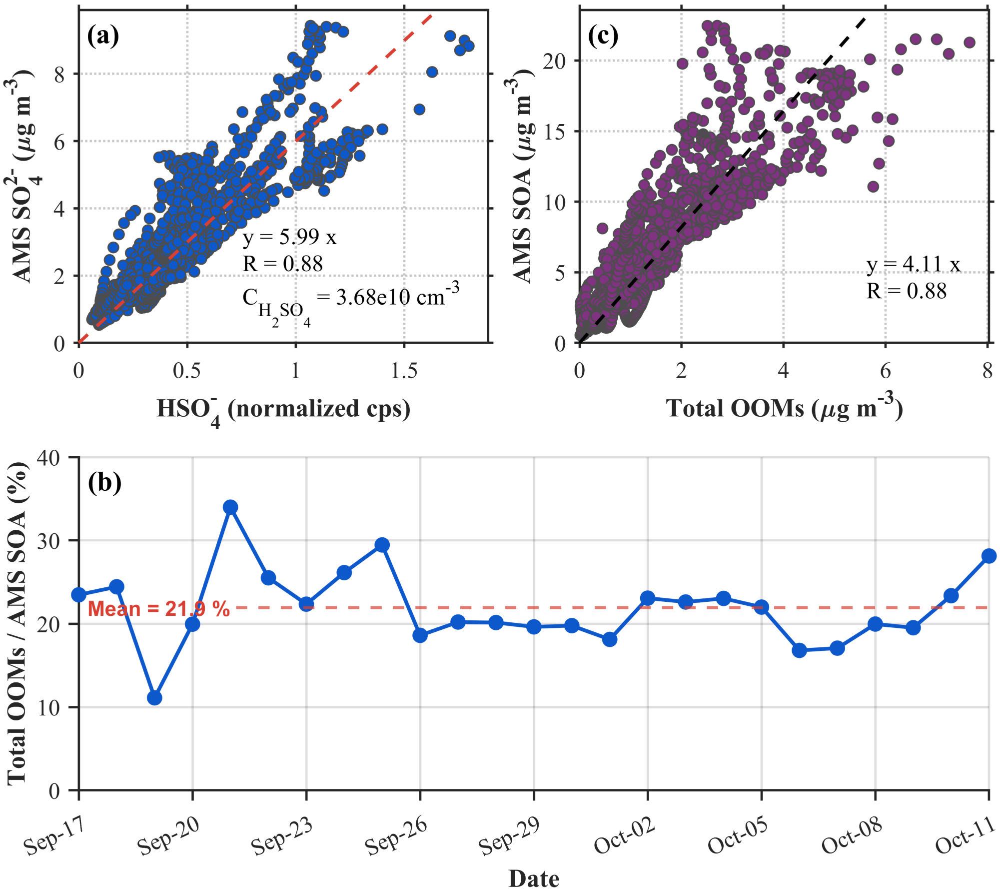

Figure S7. Empirical calibration of VIA-NO_3-CIMS measurements and comparison with AMS-derived aerosol components. (a) Correlation between normalized HSO_4^- signal measured by VIA-NO_3-CIMS and AMS sulfate concentration. (b) Temporal variation of the ratio between total particle-phase OOM concentration and AMS-derived SOA concentration during the observation period. (c) Correlation between calibrated total particle-phase OOM concentration and AMS-derived SOA concentration.

S5 Source apportionment of organic aerosol resolved by HR-ToF-AMS

The HR-TOF-AMS dataset, comprising 259 ions with m/z values between 12 and 120 from high-resolution peak fitting, was used for source apportionment. To minimize the influence of poorly constrained signals, ions with SNR < 0.2 were downweighted by a factor of 10, and those with 0.2 ≤ SNR < 2 were downweighted by a factor of 2 (Paatero & Hopke, 2003). We explored PMF solutions with 1–10 factors. The Q/Qexp ratio decreased monotonically with increasing factor number, but the statistical improvement became marginal beyond five factors (Fig. S8). Solutions with fewer than five factors tended to mix different sources, whereas those with more than five factors resulted in artificial splitting without producing additional interpretable profiles. Taking into account both statistical diagnostics and the interpretability of factor profiles and time series, the 5-factor solution was selected as the most appropriate, with the final results obtained using an fpeak value of –0.2 to enhance the separation of factor profiles and time series without introducing spurious structures.

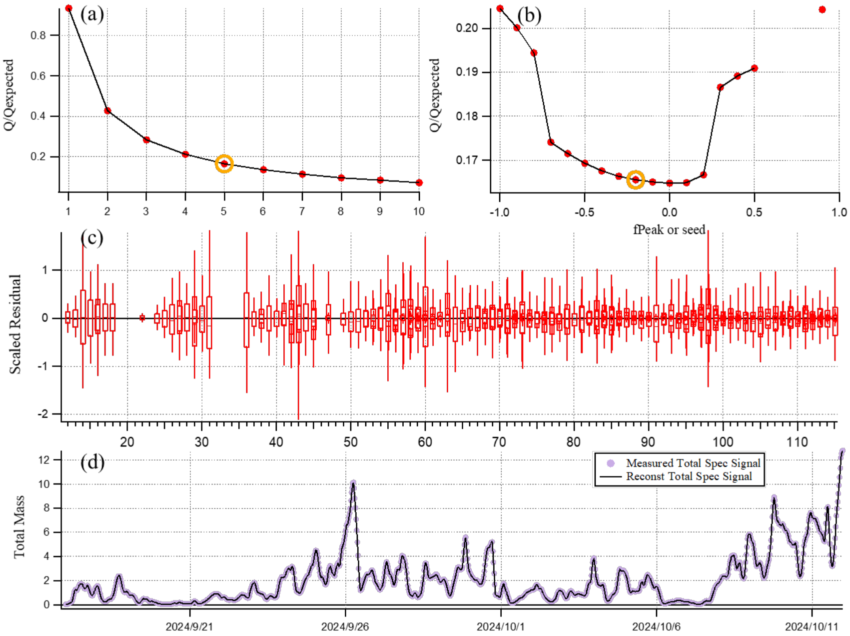

Figure S8. Diagnostic results of PMF analysis for the HR-TOF-AMS dataset. (a) Q/Qexp as a function of number of factors. (b) Q/Qexp as a function of fpeak. (c) the box and whiskers plot showing the distributions of scaled residuals for each m/z. (d) time series of the measured OA mass and the reconstructed OA mass.

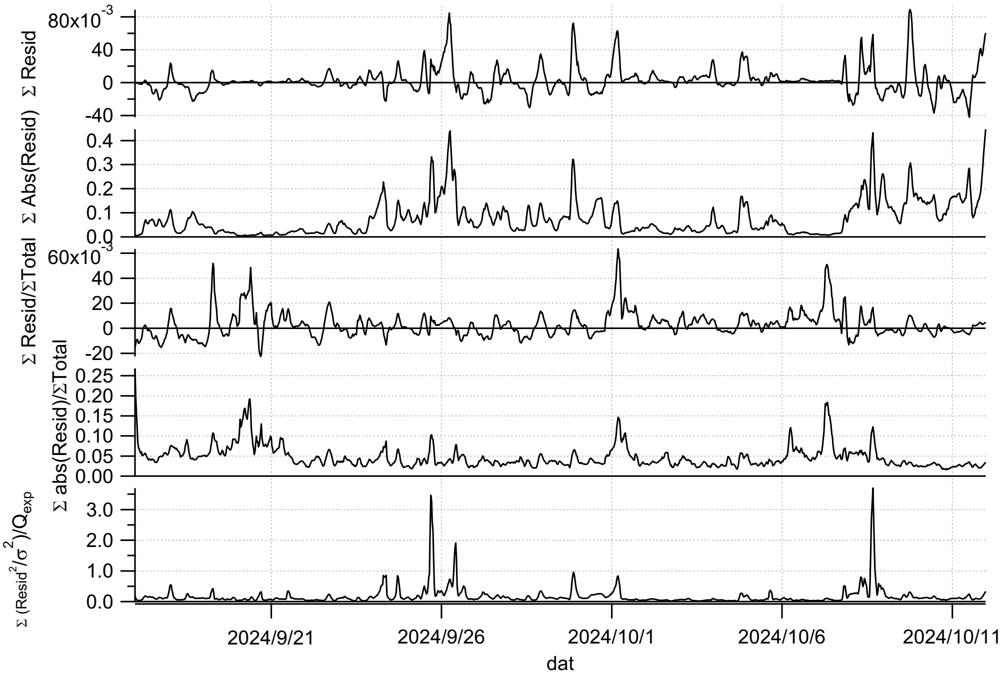

Figure S9. Distribution of scaled residuals for the 5-factor (fpeak = -0.2) solution.

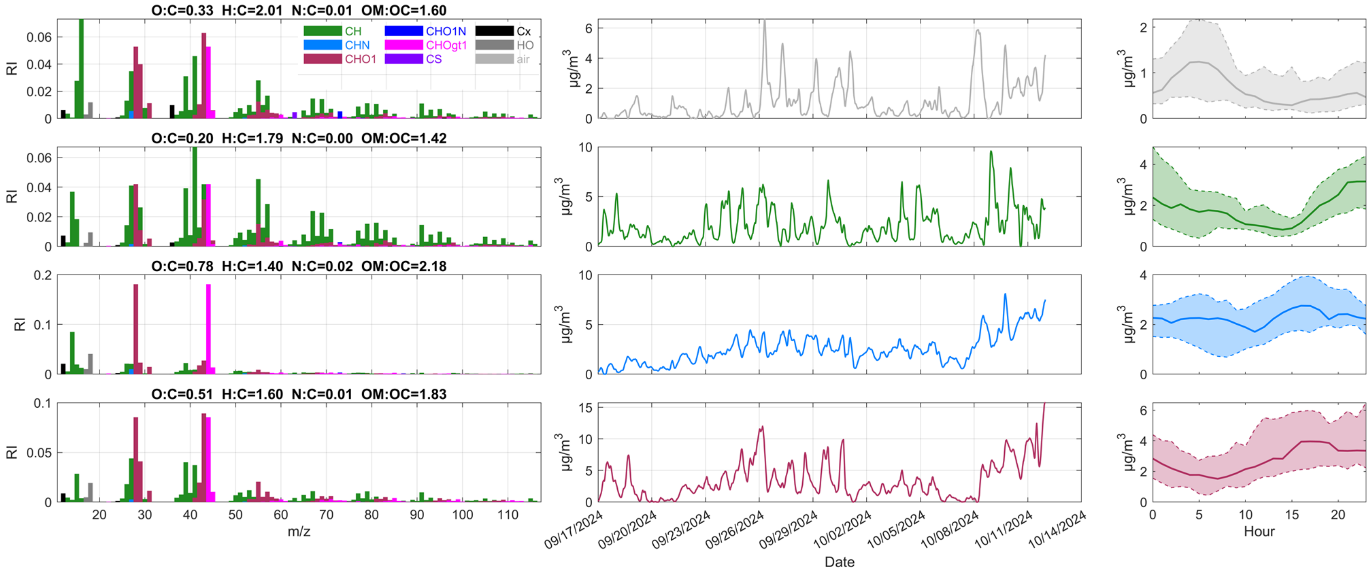

Figure S10. Source apportionment of OA measured by AMS: four-factor solution.

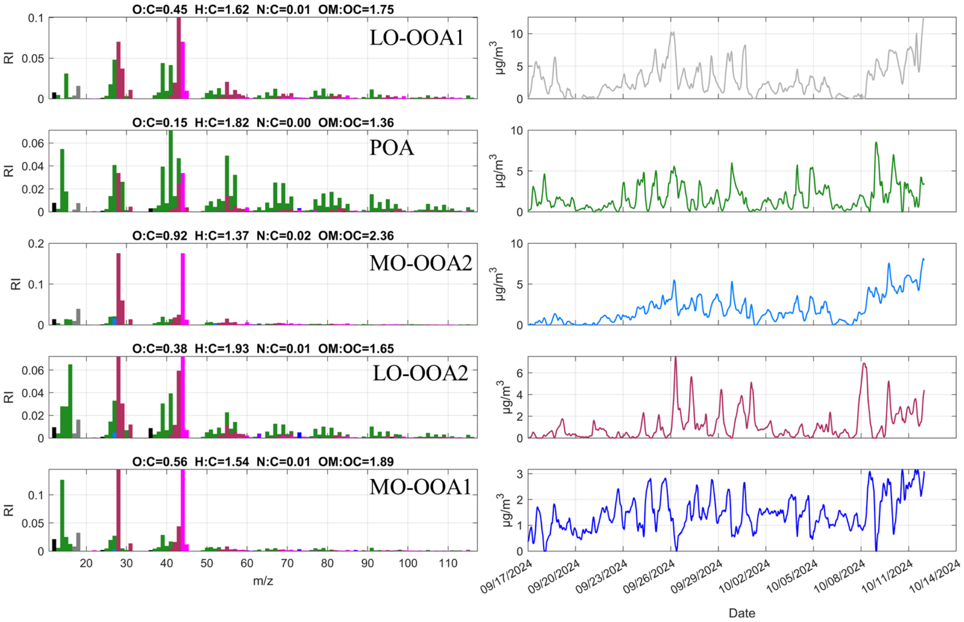

Figure S11. Source apportionment of OA measured by AMS: five-factor solution.

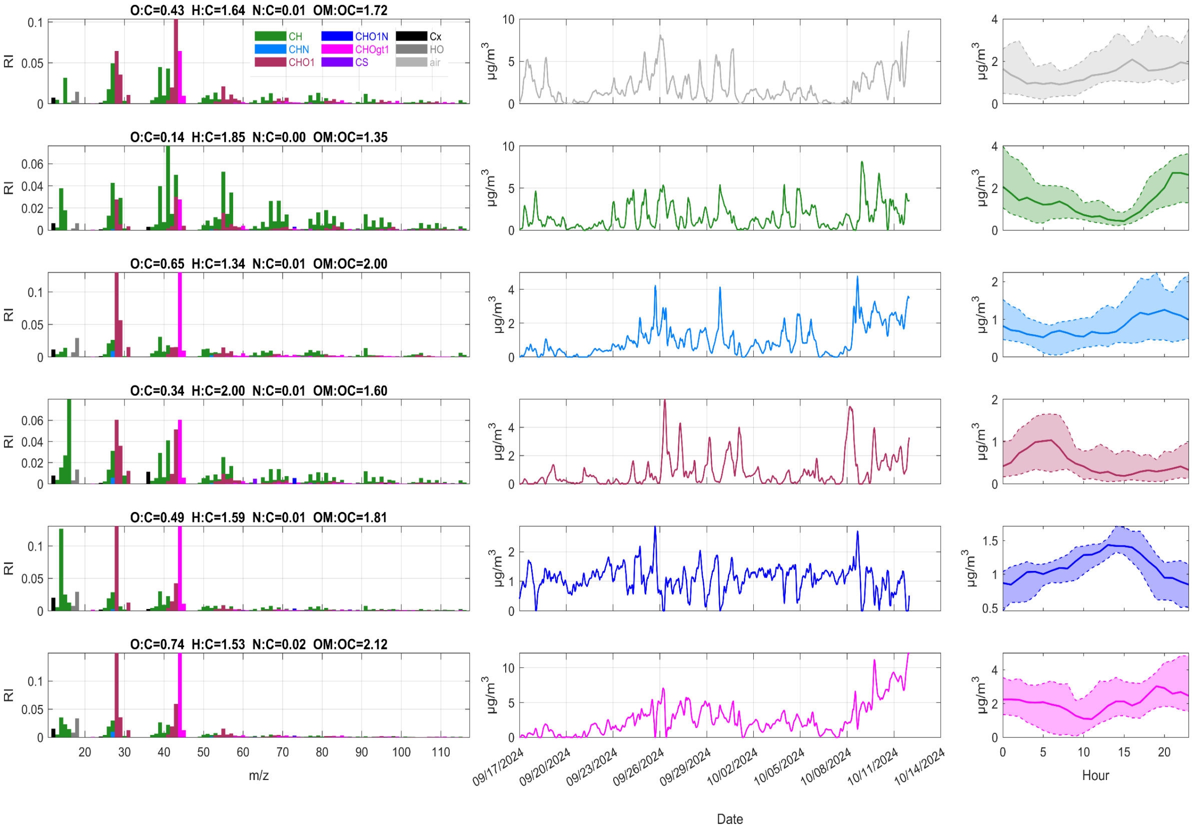

Figure S12. Source apportionment of OA measured by AMS: six-factor solution.

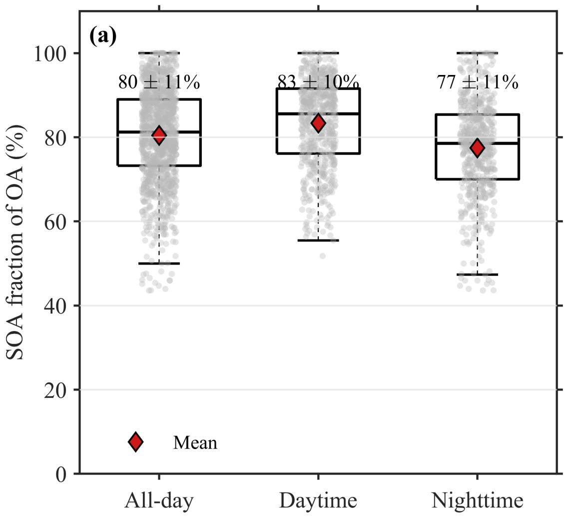

Figure S13. Distribution of SOA fraction in OA during all-day, daytime, and nighttime periods. Box plots represent the median (center line), interquartile range (box), and 5th–95th percentiles (whiskers). Gray dots indicate individual data points, and red diamonds denote mean values.

S6 Overview of VIA-NO_3-CIMS Measured Compounds

Table S1. Summary of CHO/CHON/$CHON_2$ compound classes

Class	Number	Mean concentration ($\mu g\ m^{-3}$)	Percentage (%)
CHO	1010	1.16	69.8
CHON	467	0.54	25.2
$CHON_2$	218	0.09	4.9
Total	1695	1.71	

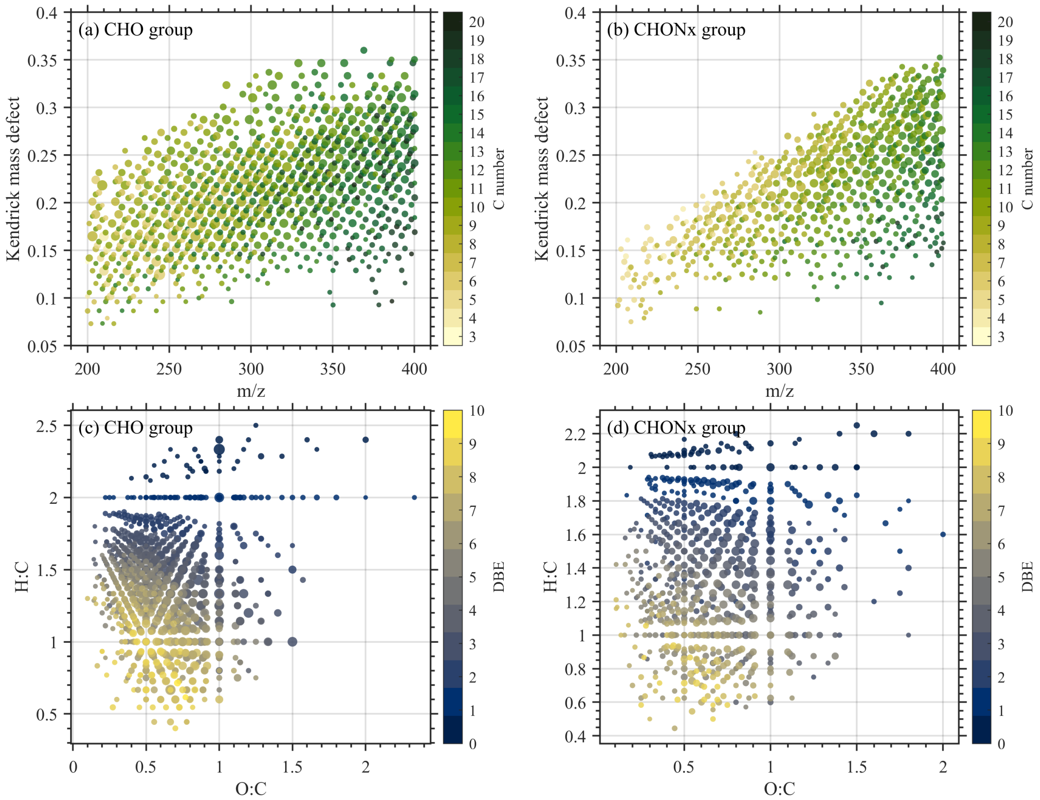

Figure S14. Kendrick mass defect (KMD) versus m/z for (a) CHO compounds and (b) $CHON_X$ compounds, colored by carbon number. Panels (c) and (d) show the corresponding Van Krevelen diagrams (H:C vs. O:C) for CHO and CHONx groups, respectively, colored by double bond equivalent (DBE). The marker size in all panels is scaled by average compound concentration.

S7 Comparison of Gaseous and Particulate Compounds

We selected the gas-phase dataset from 11–25 September 2022 as a reference for the particle-phase observations conducted during 17 September–11 October 2024. To ensure the comparability between the gas-phase organic compounds and the particle-phase compounds measured in this study, we compared the meteorological conditions of the two periods. As shown in Fig. S15, the distributions of $PM_{2.5}$ and temperature were similar, while O_3 was slightly higher during the particle-phase period; however, their interquartile ranges largely overlapped and fell within typical intra-seasonal variability. These results support the use of the 2022 gas-phase dataset as a representative seasonal reference rather than for diagnosing instantaneous gas–particle equilibrium. We then summarized the overall characteristics of the OOMs measured by NO_3-CIMS during the gas-phase period. As shown in Fig. S16, NO_3-CIMS detected a total of 1,329 OOMs, with an average concentration of 4.59×10^8 cm^{-3}. Among them, CHON species dominated both in number (466 species, 2.32×10^8 cm^{-3}) and in mass fraction (≈50.6%), followed by $CHON_2$ (196 species, 1.12×10^8 cm^{-3}, ≈24.4%) and CHO (626 species, 1.06×10^8 cm^{-3}, ≈23.1%), while $CHON_3$ contributed less than 2% (40 species, 8.53×10^6 cm^{-3}).

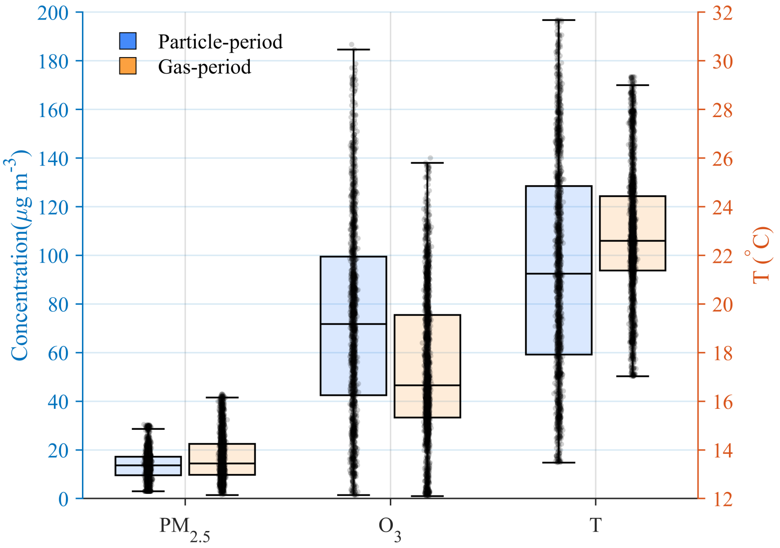

Figure S15. Comparison of background meteorological conditions ($PM_{2.5}$, O_3, and T) between the particle-phase period and the gas-phase reference period.

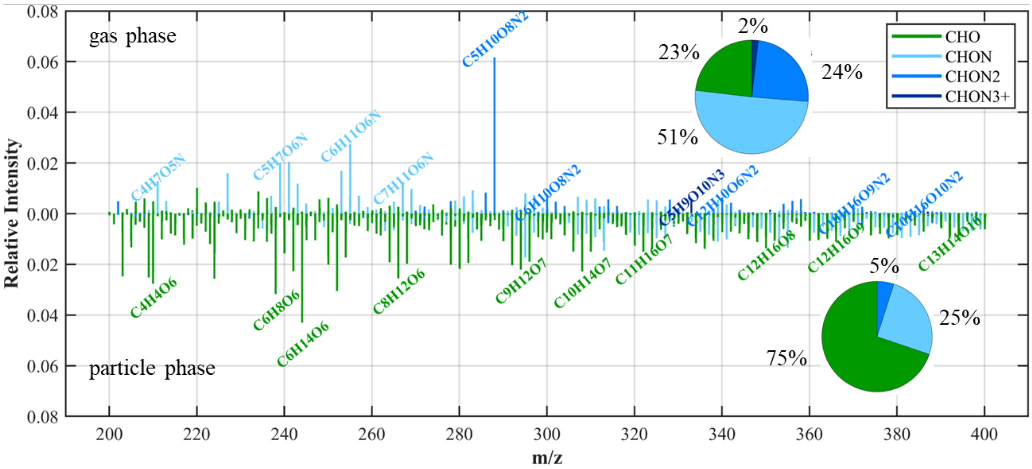

Figure S16. Mass spectra of detected organic compounds in the gas phase (top, positive axis) and particle phase (bottom, negative axis) during the measurement period. The pie charts illustrate the relative contributions of different molecular classes to the total signal in each phase.

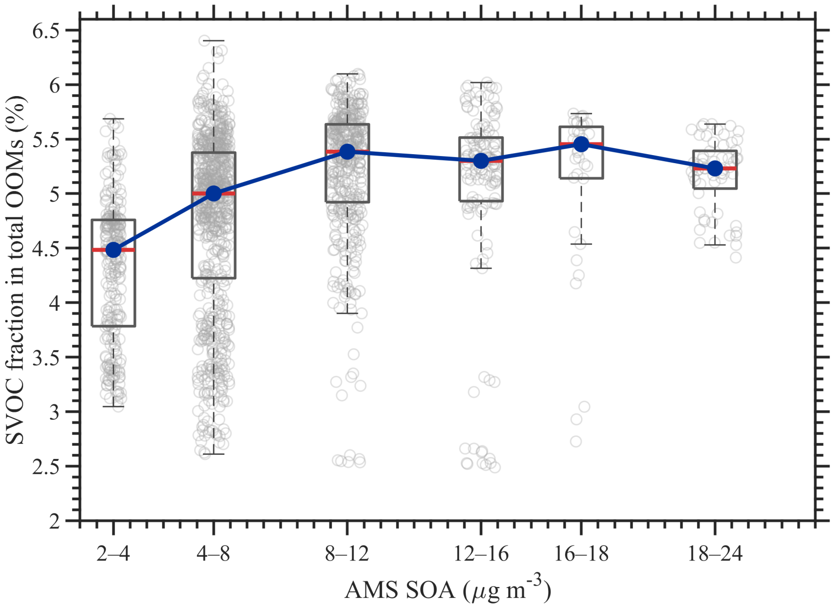

Figure S17. Variation of the SVOC fraction within total particle-phase OOMs as a function of AMS SOA loading. The data are grouped into discrete SOA bins (2–6, 6–10, 10–14, 14–18, and 18–24 μg m^{-3}). Gray circles represent individual data points, boxplots indicate the interquartile range (IQR) with median values (red lines), and whiskers denote the 5th–95th percentiles. Blue markers and connecting lines show the median SVOC fraction within each SOA bin.

S8 Calculation of molecular properties of OOMs

To evaluate the oxidation state of carbon in the observed OOMs, we adopted the method of (Kroll et al., 2011) with slight adjustments for organic nitrates. In this treatment, nitrogen atoms were considered to originate mainly from nitrate functionalities (–ONO2), which are readily detected by nitrate CI-APi-TOF. A group oxidation state of −1 was applied to -ONO2 functionality:

$$\overline{OS_C} = 2 \times (O : C - 3 \times N : C) - H : C + N : C$$

which can be rewritten as

$$\overline{OS_C} = 2 \times O : C - H : C - 5 \times N : C$$

Here, C, H, O, and N represent the number of carbon, hydrogen, oxygen, and nitrogen atoms in the molecular formula, respectively. The calculation is applicable only when the $n_C \geq 3n_N$, ensuring sufficient oxygen to accommodate the –ONO2 group. Nearly all fitted HR signals met this condition, implying that the detected nitrogen was predominantly associated with nitrate groups. It should be recognized, however, that other nitrogen-containing compounds with reduced nitrogen functionalities (e.g., amines, heterocycles, or nitrites) may still be detected if they contain enough oxygenated substituents such as –OH or –OOH.

The double bond equivalent (DBE) was used to characterize the degree of unsaturation of each detected OOM. In this study, DBE was calculated assuming that all nitrogen atoms originated from nitrate (–ONO2) or nitro (–NO2) functionalities. The DBE value reflects the combined contribution of double and triple bonds as well as cyclic structures within the molecule, and was computed as:

$$DBE = n_C + 1 - \frac{(n_H + n_N)}{2}$$

where, n_C, n_H, and n_N represent the number of carbon, hydrogen, and nitrogen atoms in the molecular formula, respectively.

The effective saturation concentration ($C*$) of the observed OOMs at 300 K was estimated using a group-contribution method introduced by (Donahue et al., 2011). The expression is given as:

$$log_{10}C^{*}(300K) = (25 - n_C) \cdot b_C - (n_O - 3n_N) \cdot b_O - nN \cdot bN - 2\frac{(n_O - 3n_N) \cdot n_C}{n_C + n_O - 3n_N} \cdot b_{CO}$$

where n_C, n_O, and n_N are the number of carbon, oxygen, and nitrogen atoms, respectively; the empirical coefficients were set to b_C= 0.475, b_O= 0.2, b_N= 2.5, and b_{CO}= 0.9. The influence of nitrate groups (–ONO2) on volatility was assumed to be comparable to that of hydroxyl (–OH) functionalities.

S9 Source apportionment of particle-phase OOMs resolved by VIA–NO_3–CIMS

In this study, we applied PMF analysis to the reconstructed CIMS dataset, testing solutions with 1–13 factors. The Q/Qexp ratio decreased monotonically with increasing factor number, but the improvement became marginal beyond seven factors, indicating diminishing statistical gains (Fig. S18). Additional factors above seven did not yield distinct or physically interpretable profiles/time series but rather reflected artificial splitting of existing factors, whereas solutions with fewer than seven factors showed mixing of different sources. Considering both statistical performance and interpretability, the 7-factor solution was selected as the most appropriate.

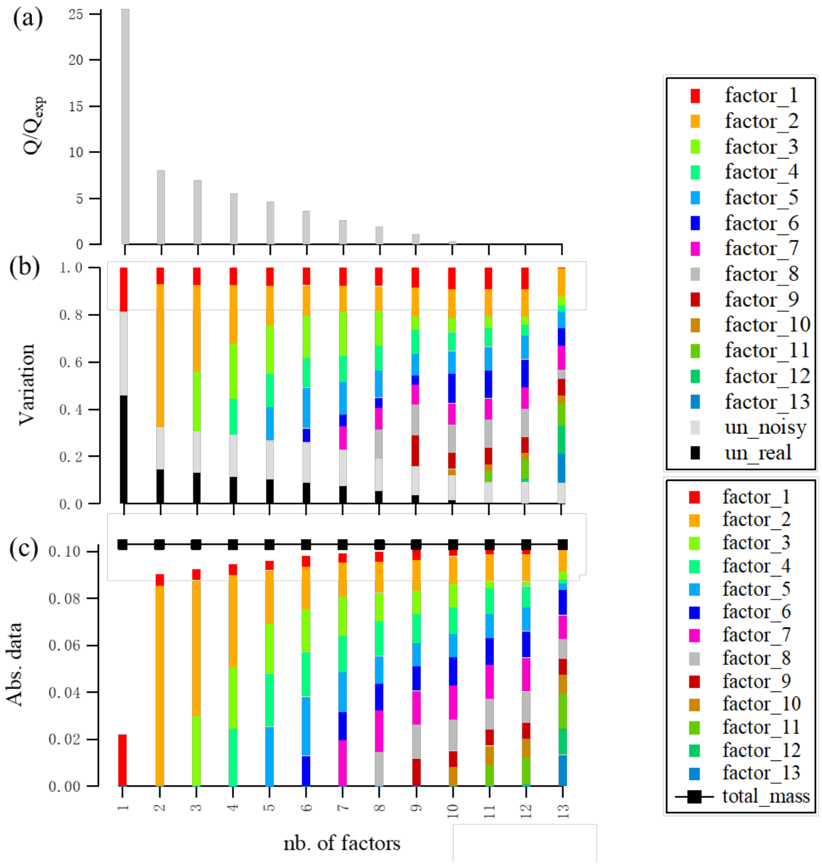

Figure S18. Diagnostics of PMF solutions, including the evolutions of (a) Q/Qexp, (b) the explained variation (EV) and unexplained variation (UEV), and (c) absolute values resolved by PMF. In (b) UEV is further separated into the real UEV for data possessing a high signal-to-noise value (un_real) and UEV for noisy data (un_noisy).

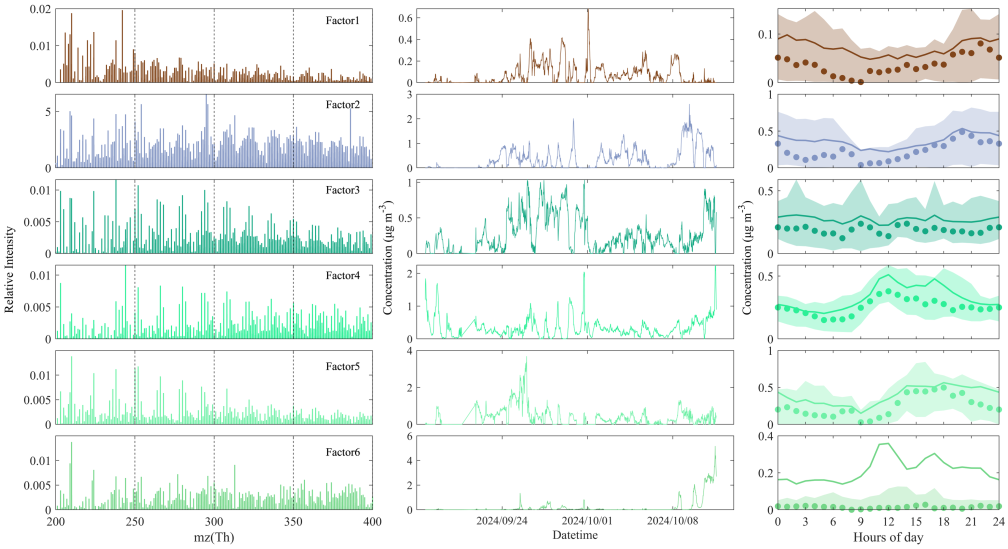

Figure S19. Source apportionment of organic compounds measured by VIA–NO$_3$–CIMS: six-factor solution. The first column shows factor profiles, the second column presents factor time series, and the third column displays diurnal variations.

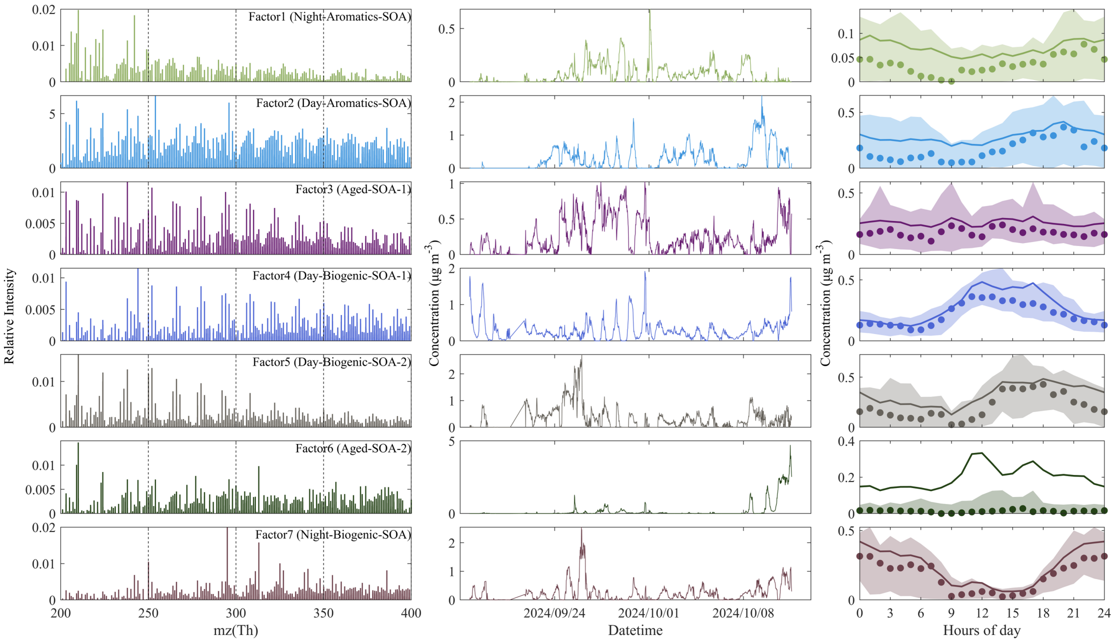

Figure S20. Source apportionment of organic compounds measured by VIA–NO$_3$–CIMS: seven-factor solution. The first column shows factor profiles, the second column presents factor time series, and the third column displays diurnal variations.

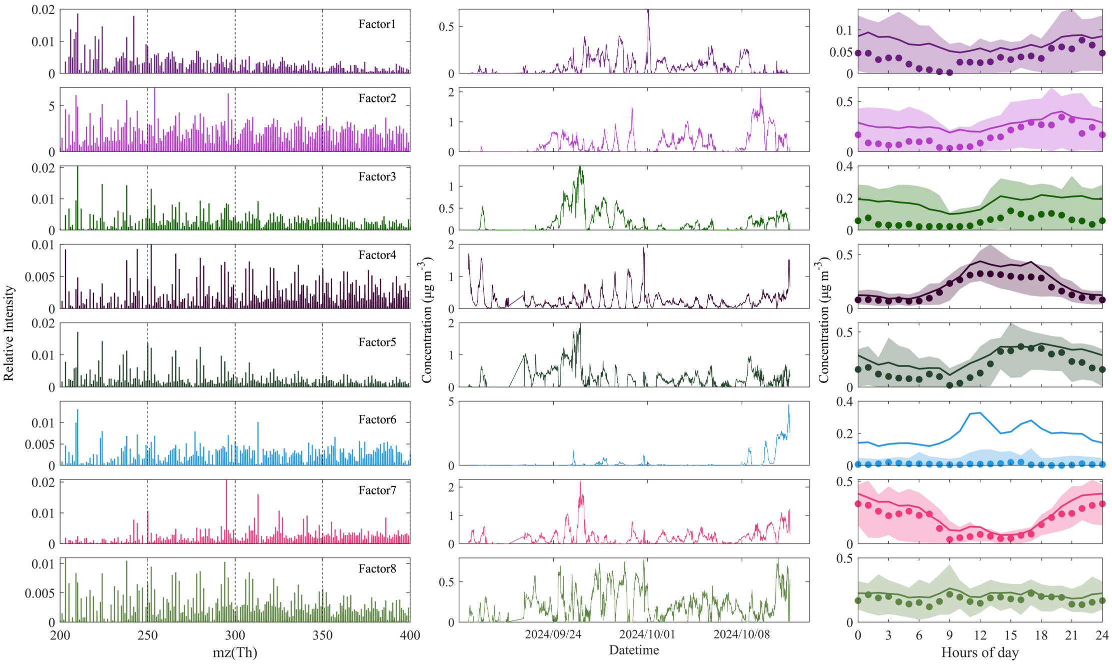

Figure S21. Source apportionment of organic compounds measured by VIA–NO_3–CIMS: eight-factor solution. The first column shows factor profiles, the second column presents factor time series, and the third column displays diurnal variations.

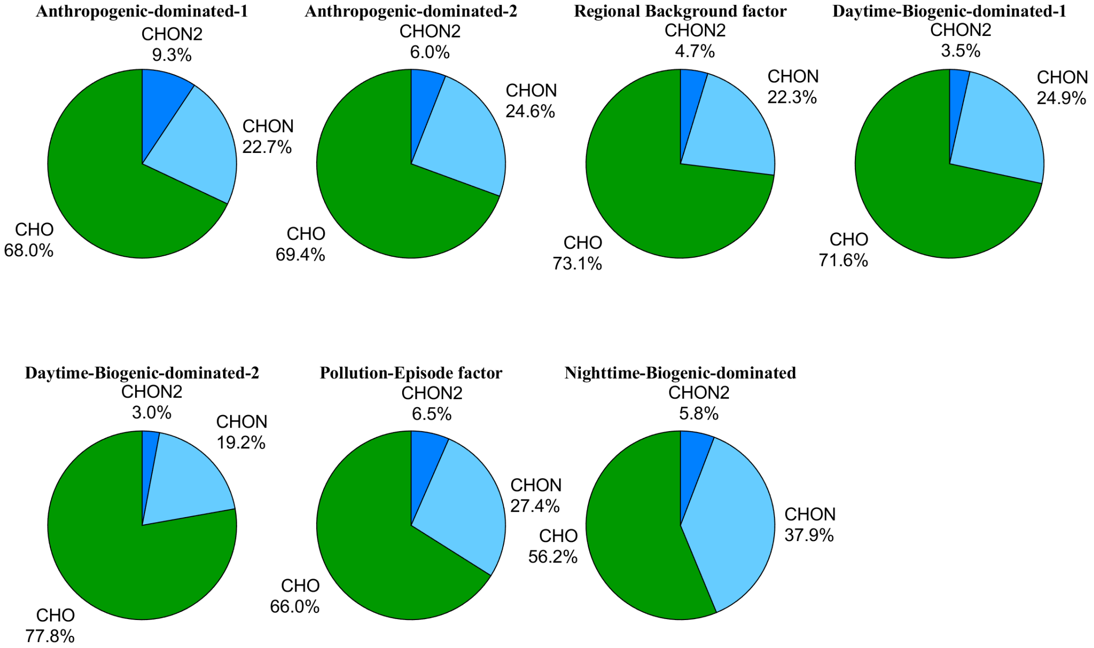

Figure S22. Compound class distribution of the seven PMF factors resolved from the CIMS dataset. Each pie chart represents one factor, with the relative contributions of CHO, CHON, and $CHON_2$ species shown as percentages of the total factor profile.

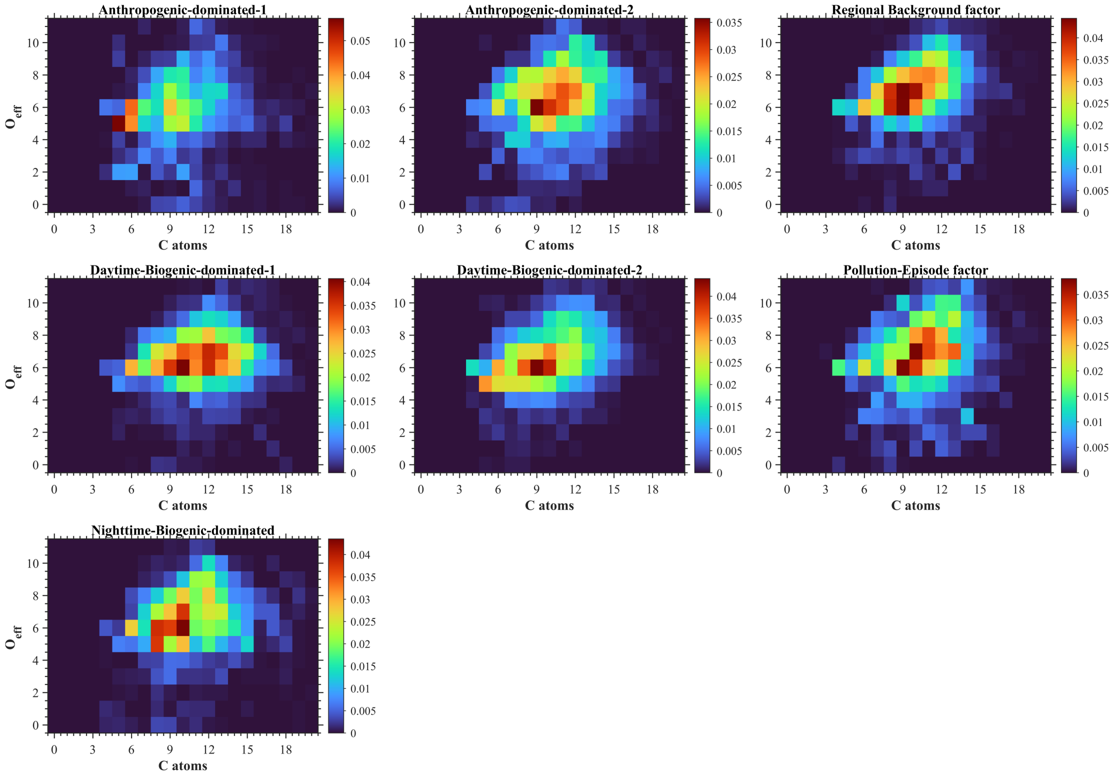

Figure S23. Two-dimensional distribution of the seven CIMS-PMF factors on the C–O atom number plane. Colors indicate relative intensities.

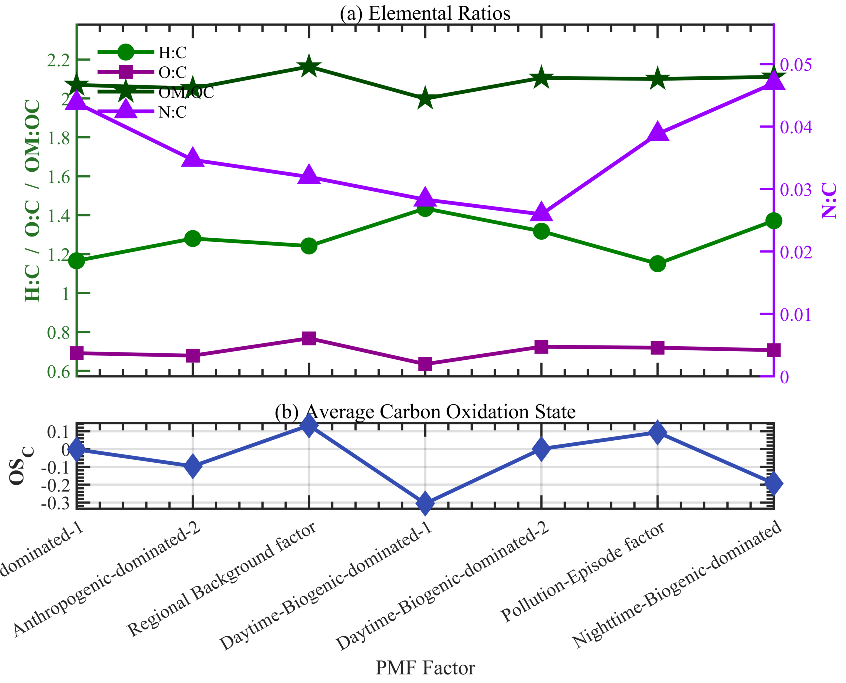

Figure S24. Elemental compositions and oxidation states of the PMF-resolved factors.

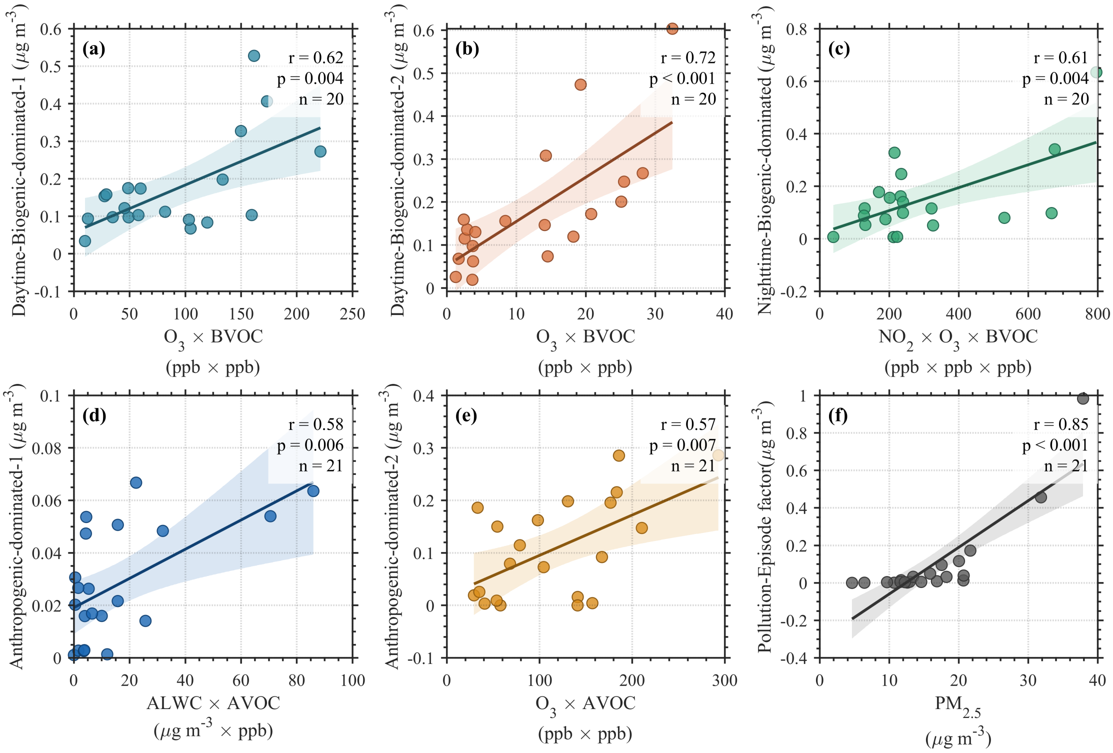

Figure S25. Correlations between PMF-resolved factors and selected proxy variables. Panels (a–c) show relationships for biogenic-dominated factors, (d–e) for anthropogenic-dominated factors, and (f) for the aged factor. Solid lines represent linear fits, and shaded areas indicate 95% confidence intervals. The correlation coefficient (r), p-value, and sample size (n) are shown in each panel.

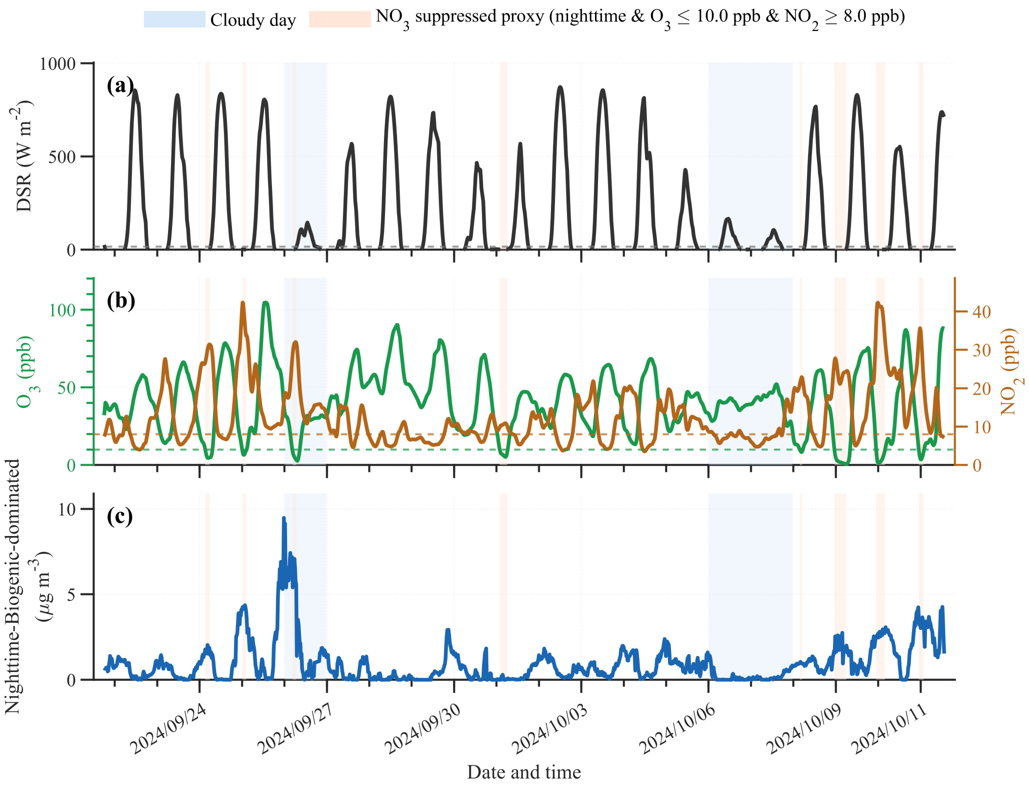

Figure S26. Time series illustrating the influence of photolysis and NO_3 availability on the Nighttime-Biogenic-dominated factor. (a) Downward solar radiation (DSR), with shaded blue regions indicating cloudy periods characterized by reduced radiation. (b) Time series of O_3 (green, left axis) and NO_2 (orange, right axis), with dashed lines marking the thresholds (O_3 = 10 ppb and NO_2 = 8 ppb) used to define NO_3-suppressed conditions. Shaded orange regions denote periods identified as NO_3-suppressed based on these criteria. (c) Time series of the Nighttime-Biogenic-dominated factor (blue).

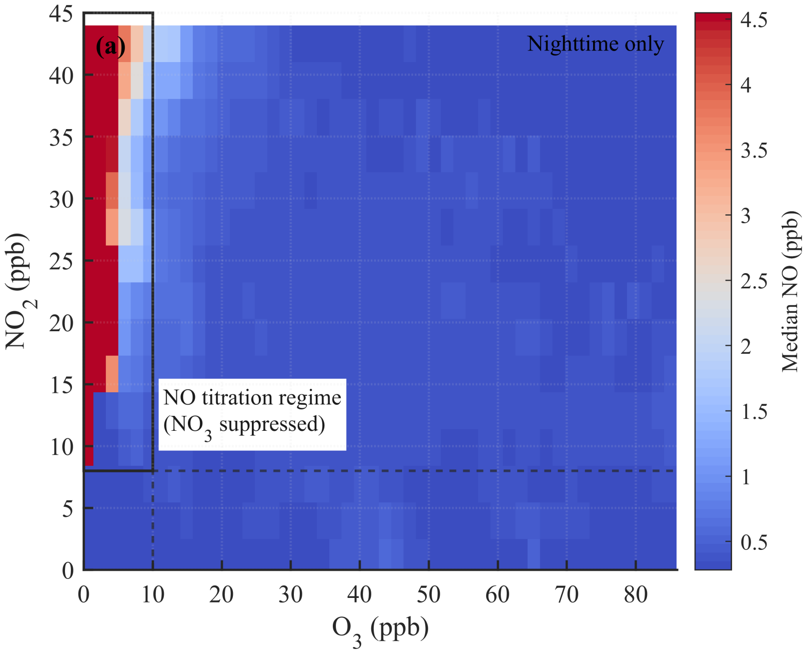

Figure S26. Median NO concentrations as a function of O_3 and NO_2 during nighttime at the SORPES site (Nanjing), based on observations from 2022. The x axis shows O_3, the y axis shows NO_2, and the color scale represents the median NO concentration (ppb) in each O_3–NO_2 bin. A distinct high-NO region is observed under low-O_3 and high-NO_2 conditions, indicating a regime in which NO_3 is expected to be efficiently suppressed through titration by NO. Based on this observed relationship, nighttime periods with $O_3 \leq 10$ ppb and $NO_2 \geq 8$ ppb are empirically defined as a proxy for NO_3-suppressed conditions (indicated by dashed lines and shaded box). Although this relationship is derived from 2022 observations rather than the 2023 study period, the similar chemical setting at the SORPES site supports the use of this classification for interpreting NO_3-related chemistry in the present study.

S10 Correction of factor contributions based on molecular constraints

In urban environments, PMF-resolved factors represent groups of compounds with similar temporal and compositional characteristics, rather than strictly source-specific emissions. As a result, factors identified as biogenic-related may include compounds whose molecular characteristics are inconsistent with typical BVOC oxidation products, such as highly unsaturated aromatic-related species or weakly functionalized aliphatic compounds.

To obtain chemically more representative estimates of biogenic-related SOA contributions, molecular-level constraints were applied during post-analysis. These constraints were implemented in a two-step framework combining literature-based identification and rule-based screening. Importantly, these procedures were applied a posteriori and did not alter the PMF solution itself.

First, a reference list of biogenic-related molecular formulas was constructed based on previous laboratory and field studies (Table S2). This list includes well-established oxidation products of BVOCs (e.g., isoprene, monoterpenes, and sesquiterpenes) formed via OH, O_3, and NO_3 oxidation pathways. Only molecular formulas observed in this study and reported in the literature were retained in this step, providing a robust anchor for biogenic SOA identification.

Second, additional molecular screening was applied to the remaining compounds based on elemental composition and structural indicators. Compounds with double bond equivalents (DBE) greater than 4 were excluded, as these highly unsaturated species are more characteristic of aromatic oxidation products and anthropogenic precursors. Compounds with DBE less than 2 were also excluded, as they typically correspond to saturated or weakly functionalized aliphatic structures. Furthermore, screening based on effective oxygen content ($O_{eff} = O - 2N$) was applied. Compounds with DBE = 2 and $O_{eff} > 6$ were excluded, as they likely represent highly oxygenated aromatic-related species rather than typical BVOC-derived products. These criteria were informed by established molecular classification frameworks (Nie et al., 2022).

Following these procedures, the retained mass fraction of each PMF factor was calculated and used to rescale the corresponding time series. The diurnal patterns remain essentially unchanged, indicating that temporal variability is preserved, while the contributions of biogenic-related factors are systematically reduced (Fig. S28). This two-step approach provides a more chemically constrained and literature-supported estimate of factor contributions.

Table S2. Representative molecular formulas identified in this study, along with their proposed formation pathways, phase classification (gas or particle), and corresponding literature references.

Molecular formula	Oxidation pathway	Phase	Reference
$C_5H_8O_{5,6,7}$	Isoprene + OH	Gas	(Krechmer et al., 2015)
$C_5H_{10}O_{6,7,8}$	Isoprene + OH	Gas	(Wang et al., 2018)
$C_5H_7O_{4,7}N$	Isoprene + NO3 + NO3	Gas	(D. Zhao et al., 2021)
$C_5H_9O_{4,6,7,9}N$	Isoprene + NO3	Gas	(D. Zhao et al., 2021)
$C_5H_{11}O_{4,7,8}N$	Isoprene + NO3 + OH	Gas	(D. Zhao et al., 2021)
$C_{10}H_{14}O_{5,6,7,8,9,10}$	α-Pinene + O3	Gas	(Claflin et al., 2018)
$C_{10}H_{16}O_{5,6,7,8,9}$	α-Pinene + O3	Gas	(Z. Zhao et al., 2021)
$C_{10}H_{18}O_{5,6,7,8,9}$	α-pinene + O3	Gas	(Z. Zhao et al., 2021)
$C_{10}H_{15}O_{5,6,7,8,9}N$	β-pinene + NO3	Gas	(Shen et al., 2021)
$C_{10}H_{17}O_{5,6,7,8,9}N$	β-pinene + NO3	Gas	(Shen et al., 2021)
$C_{10}H_{19}O_{5,6,7,8,9}N$	α-pinene + NO3	Particle	(Lee et al., 2016)
$C_{15}H_{22}O_{4,5,6,7,8,9}$	α-cedrene + O3	Gas	(Richters et al., 2016)
$C_{15}H_{24}O_{4,5,6,7,8}$	β-caryophyllonic + O3	Particle	(Gao et al., 2022)
$C_{15}H_{26}O_{5,6,7,8}$	β-caryophyllonic + OH	Particle	(Witkowski et al., 2019)
$C_{15}H_{23}O_{6,7}N$	β-caryophyllonic + NO3	Particle	(Fry et al., 2014)
$C_{15}H_{25}O_{5,6,7}N$	β-caryophyllonic + NO3	Particle	(Fry et al., 2014)
$C_8H_{12}O_6$	cis-pinonic acid + OH	Particle	(Szmigielski et al., 2007)
$C_8H_{11,13}O_{7,8}N$	β-pinene + NO3	Gas	(Shen et al., 2021)

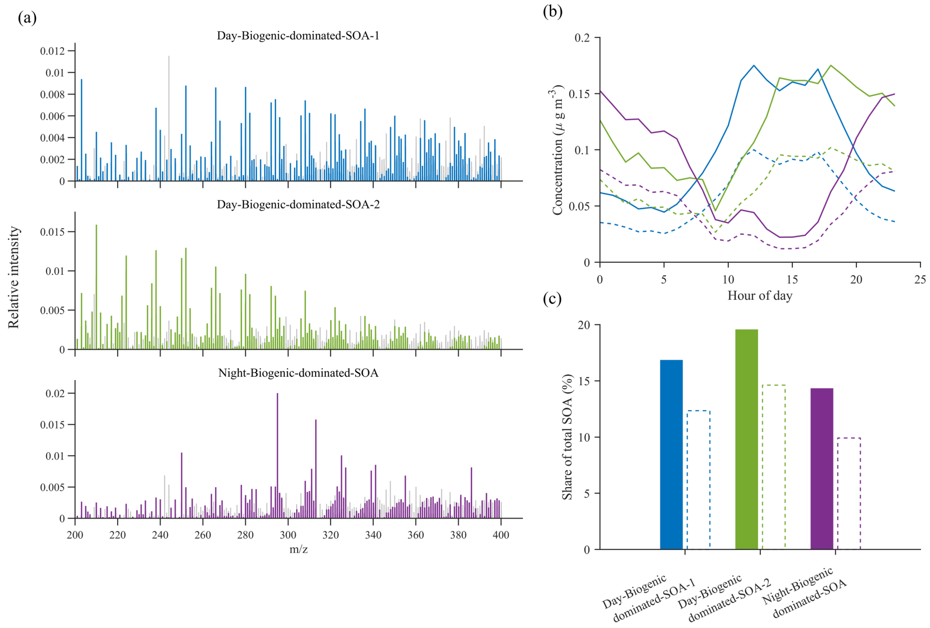

Figure S28 (a) Mass spectra of three biogenic-dominated SOA factors, with colored bars indicating ions retained after the DBE–Oeff filter and grey bars showing excluded ions. (b) Diurnal variations of the factor concentrations before (solid lines) and after (dashed lines) the DBE–Oeff screening. (c) Contributions of the three factors to total SOA before (solid bars) and after (dashed bars) the screening.

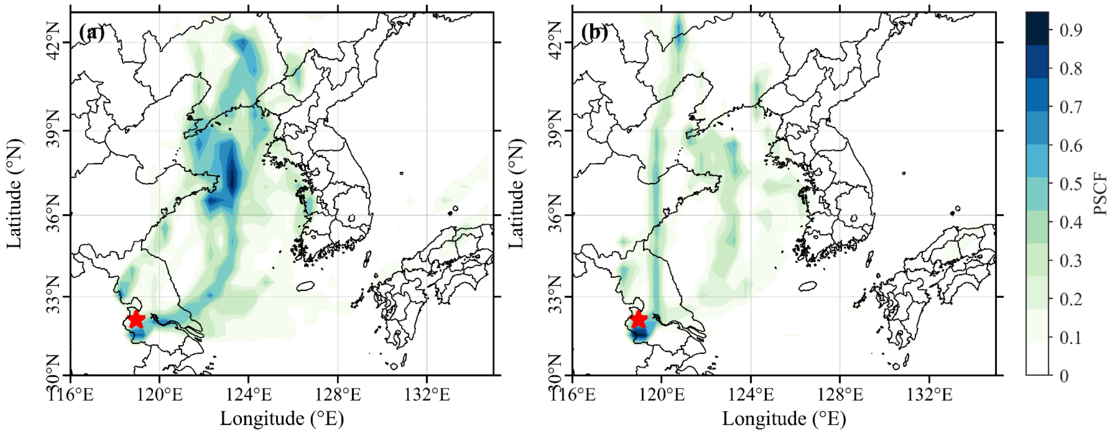

Figure S29. Potential source contribution function (PSCF) analysis results for the Regional Background and Pollution-Episode factors. Panel (a) shows the PSCF distribution of the Regional Background factor, and panel (b) shows the PSCF distribution of the Pollution-Episode factor. The color scale indicates the probability values of potential source regions, with higher values (blue) representing stronger contributions. The red star marks the receptor site location.

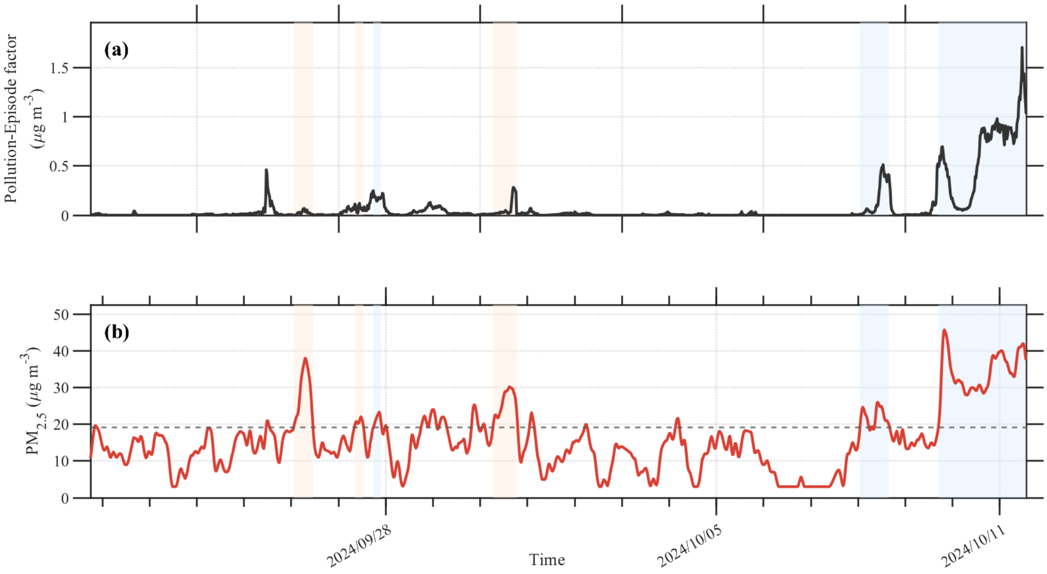

Figure S30. Time series of (a) the Pollution-Episode factor concentration and (b) $PM_{2.5}$ during the study period. Shaded regions indicate identified high-PM pollution episodes. Blue shaded regions represent High-PE episodes, characterized by concurrent enhancements of the Pollution-Episode factor and $PM_{2.5}$, whereas orange shaded regions represent Low-PE episodes, during which $PM_{2.5}$ remained elevated without a corresponding increase in the Pollution-Episode factor. The dashed line in panel (b) denotes the threshold used to define high-PM episodes.

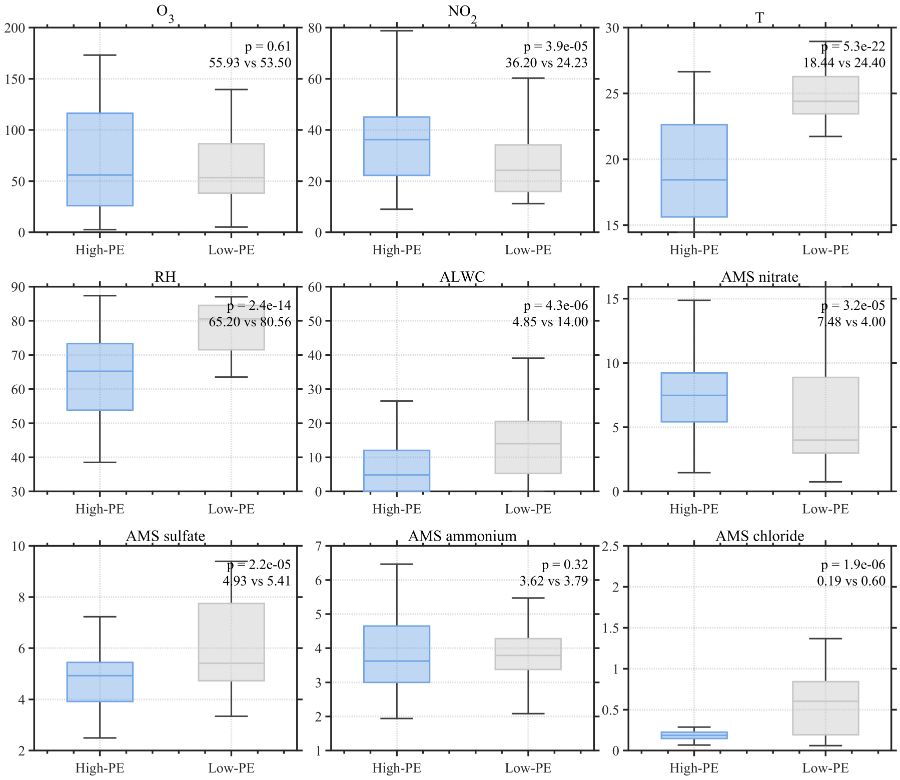

Figure S31. Comparison of key meteorological parameters, oxidants, and aerosol chemical composition between High-PE and Low-PE pollution episodes. Variables include O_3, NO_2, temperature (T), relative humidity (RH), aerosol liquid water content (ALWC), and major aerosol species. Box plots represent the distribution of each variable, with median values and statistical significance (p-values) indicated.

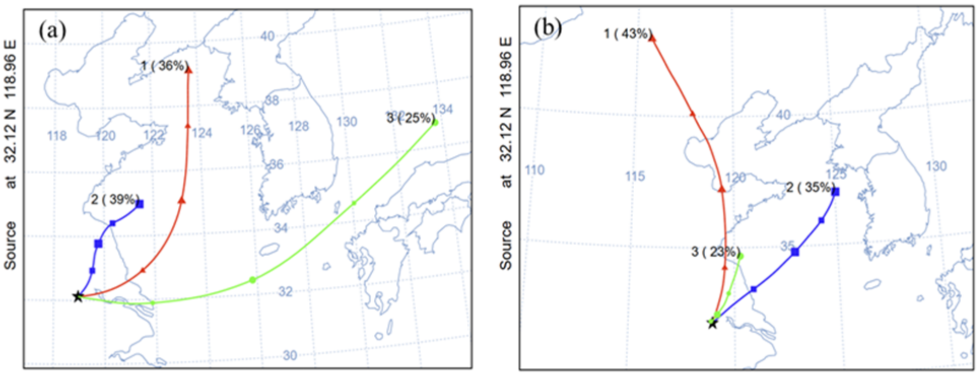

Figure S32. Clustered 48 h backward air mass trajectories arriving at the sampling site for (a) the pre-pollution period (17 September–1 October 2023) and (b) the high-pollution period after 1 October 2023. Trajectories are grouped into distinct clusters, with percentages indicating their relative contributions.

References

Allan, J. D., Jimenez, J. L., Williams, P. I., Alfarra, M. R., Bower, K. N., Jayne, J. T., Coe, H., & Worsnop, D. R. (2003). Quantitative sampling using an Aerodyne aerosol mass spectrometer 1. Techniques of data interpretation and error analysis. *Journal of Geophysical Research: Atmospheres*, *108*(D3). https://doi.org/https://doi.org/10.1029/2002JD002358

Claflin, M. S., Krechmer, J. E., Hu, W., Jimenez, J. L., & Ziemann, P. J. (2018). Functional Group Composition of Secondary Organic Aerosol Formed from Ozonolysis of α-Pinene Under High VOC and Autoxidation Conditions. *ACS Earth and Space Chemistry*, *2*(11), 1196-1210. https://doi.org/10.1021/acsearthspacechem.8b00117

Donahue, N. M., Epstein, S. A., Pandis, S. N., & Robinson, A. L. (2011). A two-dimensional volatility basis set: 1. organic-aerosol mixing thermodynamics. *Atmos. Chem. Phys.*, *11*(7), 3303-3318. https://doi.org/10.5194/acp-11-3303-2011

Fry, J. L., Draper, D. C., Barsanti, K. C., Smith, J. N., Ortega, J., Winkler, P. M., Lawler, M. J., Brown, S. S., Edwards, P. M., Cohen, R. C., & Lee, L. (2014). Secondary Organic Aerosol Formation and Organic Nitrate Yield from NO3 Oxidation of Biogenic Hydrocarbons. *Environmental Science & Technology*, *48*(20), 11944-11953. https://doi.org/10.1021/es502204x

Gao, L., Song, J., Mohr, C., Huang, W., Vallon, M., Jiang, F., Leisner, T., & Saathoff, H. (2022). Kinetics, SOA yields, and chemical composition of secondary organic aerosol from β-caryophyllene ozonolysis with and without nitrogen oxides between 213 and 313 K. *Atmos. Chem. Phys.*, *22*(9), 6001-6020. https://doi.org/10.5194/acp-22-6001-2022

Krechmer, J. E., Coggon, M. M., Massoli, P., Nguyen, T. B., Crounse, J. D., Hu, W., Day, D. A., Tyndall, G. S., Henze, D. K., Rivera-Rios, J. C., Nowak, J. B., Kimmel, J. R., Mauldin, R. L., III, Stark, H., Jayne, J. T., Sipilä, M., Junninen, H., St. Clair, J. M., Zhang, X.,…Canagaratna, M. R. (2015). Formation of Low Volatility Organic Compounds and Secondary Organic Aerosol from Isoprene Hydroxyhydroperoxide Low-NO Oxidation. *Environmental Science & Technology*, *49*(17), 10330-10339. https://doi.org/10.1021/acs.est.5b02031

Kroll, J. H., Donahue, N. M., Jimenez, J. L., Kessler, S. H., Canagaratna, M. R., Wilson, K. R., Altieri, K. E., Mazzoleni, L. R., Wozniak, A. S., Bluhm, H., Mysak, E. R., Smith, J. D., Kolb, C. E., & Worsnop, D. R. (2011). Carbon oxidation state as a metric for describing the chemistry of atmospheric organic aerosol. *Nature Chemistry*, *3*(2), 133-139. https://doi.org/10.1038/nchem.948

Lee, B. H., Mohr, C., Lopez-Hilfiker, F. D., Lutz, A., Hallquist, M., Lee, L., Romer, P., Cohen, R. C., Iyer, S., Kurtén, T., Hu, W., Day, D. A., Campuzano-Jost, P., Jimenez, J. L., Xu, L., Ng, N. L., Guo, H., Weber, R. J., Wild, R. J.,…Thornton, J. A. (2016). Highly functionalized organic nitrates in the southeast United States: Contribution to secondary organic aerosol and reactive nitrogen budgets. *Proceedings of the National Academy of Sciences*, *113*(6), 1516-1521. https://doi.org/10.1073/pnas.1508108113

Nie, W., Yan, C., Huang, D. D., Wang, Z., Liu, Y., Qiao, X., Guo, Y., Tian, L., Zheng, P., Xu, Z., Li, Y., Xu, Z., Qi, X., Sun, P., Wang, J., Zheng, F., Li, X., Yin, R., Dallenbach, K. R.,…Ding, A. (2022). Secondary organic aerosol formed by condensing anthropogenic vapours over China's megacities. *Nature Geoscience*, *15*(4), 255-261. https://doi.org/10.1038/s41561-022-00922-5

Paatero, P., & Hopke, P. K. (2003). Discarding or downweighting high-noise variables in factor analytic models. *Analytica Chimica Acta*, *490*(1), 277-289.

https://doi.org/https://doi.org/10.1016/S0003-2670(02)01643-4

Polissar, A. V., Hopke, P. K., Paatero, P., Malm, W. C., & Sisler, J. F. (1998). Atmospheric aerosol over Alaska: 2. Elemental composition and sources. *Journal of Geophysical Research: Atmospheres*, *103*(D15), 19045-19057. https://doi.org/https://doi.org/10.1029/98JD01212

Richters, S., Herrmann, H., & Berndt, T. (2016). Highly Oxidized RO2 Radicals and Consecutive Products from the Ozonolysis of Three Sesquiterpenes. *Environmental Science & Technology*, *50*(5), 2354-2362. https://doi.org/10.1021/acs.est.5b05321

Shen, H., Zhao, D., Pullinen, I., Kang, S., Vereecken, L., Fuchs, H., Acir, I.-H., Tillmann, R., Rohrer, F., Wildt, J., Kiendler-Scharr, A., Wahner, A., & Mentel, T. F. (2021). Highly Oxygenated Organic Nitrates Formed from NO3 Radical-Initiated Oxidation of β-Pinene. *Environmental Science & Technology*, *55*(23), 15658-15671. https://doi.org/10.1021/acs.est.1c03978

Szmigielski, R., Surratt, J. D., Gómez-González, Y., Van der Veken, P., Kourtchev, I., Vermeylen, R., Blockhuys, F., Jaoui, M., Kleindienst, T. E., Lewandowski, M., Offenberg, J. H., Edney, E. O., Seinfeld, J. H., Maenhaut, W., & Claeys, M. (2007). 3-methyl-1,2,3-butanetricarboxylic acid: An atmospheric tracer for terpene secondary organic aerosol. *Geophysical Research Letters*, *34*(24). https://doi.org/https://doi.org/10.1029/2007GL031338

Wang, S., Riva, M., Yan, C., Ehn, M., & Wang, L. (2018). Primary Formation of Highly Oxidized Multifunctional Products in the OH-Initiated Oxidation of Isoprene: A Combined Theoretical and Experimental Study. *Environmental Science & Technology*, *52*(21), 12255-12264. https://doi.org/10.1021/acs.est.8b02783

Witkowski, B., Al-sharafi, M., & Gierczak, T. (2019). Kinetics and products of the aqueous-phase oxidation of β-caryophyllonic acid by hydroxyl radicals. *Atmospheric Environment*, *213*, 231-238. https://doi.org/https://doi.org/10.1016/j.atmosenv.2019.06.016

Yan, C., Nie, W., Äijälä, M., Rissanen, M. P., Canagaratna, M. R., Massoli, P., Junninen, H., Jokinen, T., Sarnela, N., Häme, S. A. K., Schobesberger, S., Canonaco, F., Yao, L., Prévôt, A. S. H., Petäjä, T., Kulmala, M., Sipilä, M., Worsnop, D. R., & Ehn, M. (2016). Source characterization of highly oxidized multifunctional compounds in a boreal forest environment using positive matrix factorization. *Atmos. Chem. Phys.*, *16*(19), 12715-12731. https://doi.org/10.5194/acp-16-12715-2016

Zhang, Y., Peräkylä, O., Yan, C., Heikkinen, L., Äijälä, M., Daellenbach, K. R., Zha, Q., Riva, M., Garmash, O., Junninen, H., Paatero, P., Worsnop, D., & Ehn, M. (2019). A novel approach for simple statistical analysis of high-resolution mass spectra. *Atmos. Meas. Tech.*, *12*(7), 3761-3776. https://doi.org/10.5194/amt-12-3761-2019

Zhao, D., Pullinen, I., Fuchs, H., Schrade, S., Wu, R., Acir, I. H., Tillmann, R., Rohrer, F., Wildt, J., Guo, Y., Kiendler-Scharr, A., Wahner, A., Kang, S., Vereecken, L., & Mentel, T. F. (2021). Highly oxygenated organic molecule (HOM) formation in the isoprene oxidation by NO3 radical. *Atmos. Chem. Phys.*, *21*(12), 9681-9704. https://doi.org/10.5194/acp-21-9681-2021

Zhao, Z., Zhang, W., Alexander, T., Zhang, X., Martin, D. B. C., & Zhang, H. (2021). Isolating α-Pinene Ozonolysis Pathways Reveals New Insights into Peroxy Radical Chemistry and Secondary Organic Aerosol Formation. *Environmental Science & Technology*, *55*(10), 6700-6709. https://doi.org/10.1021/acs.est.1c02107